Journal of
Marine Science and Engineering

MDPI

Article

An Enhanced Wave Estimation Approach by Combining Statistical Linearization and Prolate Spheroidal Wave Functions

Malwin Wermbter [1], Jian Tan [2,*] and Moustafa Abdel-Maksoud [1]

[1] Institute for Fluid Dynamics and Ship Theory, Hamburg University of Technology, 21073 Hamburg, Germany; malwin.wermbter@tuhh.de (M.W.); m.abdel-maksoud@tuhh.de (M.A.-M.)
[2] Faculty of Civil Engineering and Geosciences, Delft University of Technology, 2628 CN Delft, The Netherlands
* Correspondence: j.tan-2@tudelft.nl

Abstract

Phase-resolved wave estimation during operation of floating structures based on motion measurements provides an efficient, low-cost approach to enhancing operations. Prolate spheroidal wave functions (PSWFs) enable the reconstruction of wave profiles in short time windows with the help of a wave-to-motion response amplitude operator (RAO). Although fully linear hydrodynamic modeling can efficiently derive the RAO of floating structures, its applicability is highly limited to rather linear operation conditions. This study extends the PSWF methodology for wave estimation by combining it with the statistical linearization approach, which allows nonlinearities to be incorporated into the RAO based on the measured motion. The combined methodology is verified with motions for a floating cylinder and sphere, whose motions were calculated using a time domain simulation based on Cummins equation. Viscous drag and nonlinear hydrostatic forces were investigated. The results showed that the combined methodology increased the accuracy of the resulting wave profiles, measured in terms of correlation and spectral differences. Combining PSWFs and statistical linearization reproduced wave profiles with correlation values above 0.9 in waves with periods greater than 9 s. Combining both nonlinear effects for the sphere slightly increased the method's accuracy due to the reduced motion amplitudes.

Keywords: wave estimation; hydrodynamic modeling; statistical linearization; phase-resolved wave prediction; nonlinear motions

1. Introduction

In offshore and maritime engineering, real-time wave estimation is a key requirement for predicting and controlling system motions, loads, and power. Moreover, knowledge of wave profiles, in combination with arbitrary measured values (e.g., motions, loads, and power), enables valuable insights into operational behavior, the prediction accuracy of numerical tools, and long-term statistics for floating structures in complex sea environments.

On a floating platform, wave estimations may be obtained from a wave radar or buoys upstream. Both options are not generally available or cheap [1]. Floating structures respond to wave excitation, enabling the reconstruction of incident waves from motion measurements and simulated motion characteristics. Among the available methods for wave estimation, two main categories can be distinguished: data-driven methods and physics-based methods. Data-driven methods are compared by Cademartori et al. [2], who found that these methods allow for the reconstruction of waves but only with good representation of the operating conditions in the input data. Physics-based methods, represented

Check for updates

Academic Editor: Lev Shemer

Received: 7 April 2026
Revised: 24 April 2026
Accepted: 27 April 2026
Published: 29 April 2026

Copyright: © 2026 by the authors. Licensee MDPI, Basel, Switzerland. This article is an open access article distributed under the terms and conditions of the Creative Commons Attribution (CC BY) license.

by Kalman-Filter-based methods and response amplitude operator (RAO)-based methods, employ the knowledge of motion behavior from numerical simulations. Methods relying on a Kalman-Filter [1,3] require a calibration phase. RAO based methods [4–7] make use of prolate spheroidal wave functions (PSWFs), which are applicable without calibration. PSWF methods are nonetheless bound by the accuracy of the RAO obtained from either numerical models or experimental results.

RAO-based wave estimation methods have been receiving increasing research interest [4,7]. The identification of RAOs relies on understanding the dynamic behaviors of floating structures. Numerical modeling is a key tool in predicting the dynamics of floating structures, providing a resource- and time-efficient alternative to experimental and sea-trial approaches [8]. It enables the analysis of dynamic behavior and power performance across diverse floating system designs, supporting the exploration of design–performance relationships and iterative improvements toward cost-effective technologies. Common numerical approaches include linear frequency-domain (FD), Cummins equation-based time-domain (TD), and Navier–Stokes equation-based Computational Fluid Dynamics (CFD) modeling [9]. CFD offers high-fidelity simulations of nonlinear flow phenomena but is computationally demanding, making it best suited for short-duration, extreme-condition analyses such as survivability assessments [10]. TD modeling, based on the Cummins equation [11], achieves a balance between accuracy and computational efficiency by including relevant nonlinear functions. FD modeling, on the other hand, uses harmonic analysis to represent system responses in the frequency domain. Although computationally efficient, its assumption of full linearity limits its applicability [12].

TD and FD modeling methods require a fixed set of parameters defining the operational conditions. These parameters include the mass distribution, damping parameters, and operational parameters, which include water depth, marine growth, and current. In practice, accurate knowledge of all parameters is rarely available. Therefore, methods adapting an initial guess of the RAO are usually favorable for application during operation. Tuning of the RAO based on the weather data and motion measurements is possible but requires highly accurate weather data and obtaining robust RAOs in short-crested seaways is complex [13,14]. To bridge the gap between TD and FD modeling, the statistical linearization (SL) method has emerged as a promising alternative. It combines efficiency with the capacity to represent nonlinear effects in the RAO using statistical linearization. Early applications of the SL approach in floating renewable energy systems addressed quadratic damping and excitation force decoupling in oscillating-surge WECs [15], showing strong agreement with nonlinear TD models in power capture and response spectra. Later studies extended SL to include additional nonlinearities such as damping [16], end-stop mechanisms, mooring stiffness, Coulomb damping, nonlinear hydrostatic force, and machinery force capping [17–21]. A recent advancement in Tan et al. [22] has expanded the method to encompass nonlinearities throughout the full wave-to-wire process, covering both hydrodynamic and power conversion phases. More recently, the theoretical framework of the SL approach has been further extended to address multi-variate non-differentiable nonlinear effects involved in offshore renewable energy systems [23].

As discussed above, the accuracy of the applied RAO of the dynamic responses is important for accurate wave estimation within the PSWF algorithm. The high computational efficiency and inclusion of nonlinearities make the SL approach a potential solution for improving the existing PSWF applications that rely on RAOs. Although the SL approach has received notable attention as an efficient design tool for evaluating load and dynamic motions of floating structures, its applicability for integration into wave estimation algorithms has never been demonstrated.

This study proposes a combination of the SL and PSWF algorithms for wave estimation (PSWF-SL). The existing algorithms for PSWFs from Takami et al. [4] and SL from Tan et al. [23] are executed sequentially for short time windows, and accuracy is ensured by iterating the solutions until convergence is achieved. Compared to the methodology from Wermbter et al. [7] and Takami et al. [4], the extension with SL enables adaptation to the RAO during operation without requiring a database of RAOs. Therefore, it avoids interpolation errors between database entries and increases accuracy to yet unknown operational conditions which, due to increased complexity, can not be included in the PSWF methodology. The methodology is verified by applying it to a floating cylinder subject to viscous drag and to a floating sphere subject to nonlinear hydrostatics in TD. The motions are calculated using a TD solver based on the Cummins equation. Various wave heights and periods are incorporated to verify that the developed procedure is beneficial for FD calculations.

This study is organized as follows. Section 2 contains the theoretical description of the SL approach, PSWFs, and the combined approach. Section 3 is split into the results for the cylinder and the sphere, where a short description of each data set is included before the results and the discussion of the combined methodology are presented. Section 4 summarizes the contributions of this study and provides recommendations for future work.

2. Methodology

2.1. Dynamic Modeling of Floating Structures

Three different dynamic modeling approaches are applied as a comparison to predict the wave elevation based on the floater's motion. These three modeling approaches are nonlinear TD modeling, linear FD modeling, and the SL approach.

2.1.1. Nonlinear Time Domain Modeling

The motion of floating structures in the TD is commonly represented by the Cummins equation [11]:

$$[M + M_{\mathrm{r}}(\infty)]\ddot{z}(t) = F_{\mathrm{e}}(t) + F_{\mathrm{mooring}}(t) + F_{\mathrm{vis}}(t) + F_{\mathrm{hs}}(t) + F_{\mathrm{ext,non}}(t) + \int_{-\infty}^{t} K_{\mathrm{rad}}(t-\tau)\,\dot{z}(\tau)\,d\tau\,, \tag{1}$$

where

M : mass of the floating structure;
$M_{\mathrm{r}}(\infty)$: added mass at infinite frequency;
$z, \dot{z}, \ddot{z}$: displacement, velocity, and acceleration of the floater;
t : time;
F_{e} : wave excitation force;
F_{mooring} : linear mooring force;
F_{hs} : hydrostatic restoring force;
F_{vis} : viscous drag force;
K_{rad} : radiation impulse function;
τ : intermediate variable in the convolution integral;
$F_{\mathrm{ext,non}}$: nonlinear external forces.

The term $F_{\mathrm{ext,non}}$ accounts for external forces added as corrections to the Cummins equation. However, it cannot accurately capture strongly nonlinear effects such as vortex shedding. As the floater dynamics are evaluated deterministically at each time step, the nonlinear term $F_{\mathrm{ext,non}}$ can be included directly in the TD model.

2.1.2. Linear Frequency Domain Modeling

Assuming linearity, the motion of the floating structure in the frequency domain is expressed as follows:

$$\hat{F}_{\mathrm{e}}(\omega) = \hat{z}(\omega)\left\{-\omega^2\left[M + M_{\mathrm{r}}(\omega)\right] + K_{\mathrm{mooring}} + K_{\mathrm{hs}} + \mathrm{i}\omega\left[R_{\mathrm{r}}(\omega) + R_{\mathrm{vis}}\right]\right\}, \tag{2}$$

where

$\hat{F}_{\mathrm{e}}$: complex amplitude of excitation force;

ω : angular frequency;

$\hat{z}$: complex amplitude of displacement;

K_{mooring} : mooring stiffness coefficient;

K_{hs} : hydrostatic stiffness coefficient;

R_{r} : radiation damping coefficient;

R_{vis} : constant viscous damping coefficient.

The FD modeling approach is widely used for analyzing linear systems. However, as it relies on harmonic analysis, nonlinear terms are therefore neglected, as shown in (2).

2.1.3. Statistical Linearization Approach

The SL approach is built as an extension of the FD modeling approach, while nonlinear effects can be incorporated by additional equivalent terms. The equation of motion of the SL approach is expressed as

$$\hat{F}_e(\omega) = \hat{z}(\omega)\left\{-\omega^2\left[M + M_r(\omega)\right] + K_{eq,ext} + K_{hs} + K_{mooring} + \mathrm{i}\omega\left[R_r(\omega) + R_{eq,ext}\right]\right\}, \tag{3}$$

where

$K_{\mathrm{eq,ext}}$: equivalent linearized coefficient for nonlinear stiffness effects;

$R_{\mathrm{eq,ext}}$: equivalent linearized coefficient for nonlinear damping effects.

The derivation of the equivalent linearized coefficients is described in Appendix A. In more detail, the mathematical proof and derivation of the SL method have been comprehensively demonstrated in [24]. The SL method is inherently established based on the assumption that ocean waves and the floater follows the Gaussian distribution. It is known that the assumption might be challenged when nonlinear effects tend to be highly pronounced, while this approach is primarily applied to non-extreme waves in this work. Further justification of the Gaussian assumption can be found in Section 3.4 and Appendix A. Moreover, it should be noted that the equivalent linearized coefficients $K_{\mathrm{eq,ext}}$, $R_{\mathrm{eq,ext}}$, and $R_{\mathrm{eq,vis}}$ are frequency-independent and are related to statistical estimates of the system responses. An iterative algorithm is applied to solve (3) since the linearized coefficients are unknown prior to the solution of the responses.

2.1.4. Implementation of Numerical Dynamic Models

The hydrodynamic coefficients, including excitation force, radiation damping, and added mass, of floating structures applied in this work are obtained through numerical simulations using the open-source Boundary Element Method (BEM) solver, as seen in Nemoh [25]. Irregular waves are adopted in this work to better represent realistic ocean wave conditions. The irregular waves are constructed by means of the superposition of harmonic wave components based on the JONSWAP wave spectrum [26]. Each irregular wave train contains 1000 frequency components with randomly distributed phases each with an individual seed, and the frequencies range from 0.1 $\frac{\text{rad}}{\text{s}}$ to 3 $\frac{\text{rad}}{\text{s}}$. In the present study, long-crested seaways are used to verify the applicability of the proposed approach. Calculations with short-crested seaways is possible, but they generally reduce the accuracy due to the spreading of wave energy as shown by Takami et al. [5]. In the SL approach, the iterative scheme is used to solve the equation of motion with the solution of the linear FD model as the initial guess, and the convergence criteria is defined as 0.01% for all the considered simulation cases [16,18].

For comparison, the linear FD and nonlinear TD modeling are also carried out to derive the response amplitude operator (RAO) which is further used to support wave prediction. Due to its higher modeling fidelity, TD modeling is adopted as the accuracy reference. The TD model is derived based on Cummins' equation, as given in (1), where the radiation force convolution term is efficiently approximated using a state-space representation based on the methodology proposed in Perez and Fossen [27]. The differential equations are numerically solved in MATLAB R2026a using the ODE45 solver, with the time step defined as 0.1 s. In this study, the ODE45 solver is employed with tolerance settings defined as a relative tolerance of 10^{-3} and an absolute tolerance of 10^{-6}. All simulations were verified to have converged with respect to the chosen time step. Since the floater's dynamics are strongly inertia-dominated, the use of ODE45 with a fixed time step is sufficient to achieve good temporal convergence. However, a variable time step approach may be more appropriate for systems exhibiting more dynamic behavior. Moreover, this TD modeling has been verified against another high-fidelity model, as shown in Tan et al. [28], demonstrating its accuracy. Each TD simulation spans 1000 s in total, of which the initial 100 s are defined as the ramping period to avoid strong transient energy flow [29], and the response results during the ramping period are therefore excluded from subsequent analysis.

2.2. Phase-Resolved Wave Prediction with PSWFs

Prolate spheroidal wave functions are used to reconstruct input motions. The PSWFs are capable of reconstructing motions even with short time windows without requiring periodicity in the considered time window. The procedure is established by Takami et al. [4] and simplified as follows for motion measurements from a single degree of freedom (DOF).

Input motions are split into time windows. Since the accuracy of the PSWFs reduces at the start and end of the time window, the windows overlap by 20% of the total time window size $2T$. The window size $2T$ is set to 4 min in the present study. Motions $z(t)$ are reconstructed with the power spectral density $S(\omega)$ and phase components $u, \bar{u}$ which are both dependent on the motion frequency ω

$$z(t) \approx \sum_{i=1}^{n} \sqrt{S(\omega_\mathrm{i})\Delta\omega}\left(u_\mathrm{i}\cos(\omega_\mathrm{i}t) - \bar{u}_\mathrm{i}\sin(\omega_\mathrm{i}t)\right). \tag{4}$$

The detailed determination of the phase components can be found in Takami et al. [4]. The number of used frequencies depends on two input parameters: the time window size $2T$ and the maximal frequency ω_max, which should be reconstructed. In this study, ω_max is set to 2 $\frac{\text{rad}}{\text{s}}$, and the frequency step size $\Delta\omega$ is set to 0.01 $\frac{\text{rad}}{\text{s}}$. Boyd [30] suggests that the number of frequencies is increased by 30 frequencies to avoid unstable PSWFs with

$$n = 2\left(\frac{2T\omega_\mathrm{max}}{\pi} - 1\right) + 30. \tag{5}$$

The power spectrum is calculated with the help of the autocorrelation function γ:

$$S(\omega_\mathrm{i}) = \frac{2}{\pi} \int_0^{2T} \gamma(\tau) \cos(\omega_\mathrm{i} \tau) \, \mathrm{d}\tau \,. \tag{6}$$

The autocorrelation function is beneficial because it resembles the phase information with higher accuracy than Fourier analysis. It is calculated from the time series as follows:

$$\gamma(t_\mathrm{k}) = \frac{\sum_{i=0}^{N-k-1} (z(t_{\mathrm{i+k}}) - \mu)(z(t_\mathrm{i}) - \mu)}{\sum_{i=1}^{N-1} (z(t_\mathrm{i}) - \mu)^2} \,, \tag{7}$$

with the time window mean value μ.

The complex RAO $\hat{Y}$ of a floating structure is typically used to calculate linear motions from the known waves $\zeta(\omega, t)$ or their wave spectrum $S_\zeta(\omega)$. Takami et al. [4] solved the inverse problem, which, for one DOF, is simply as follows:

$$S_\zeta(\omega_\mathrm{i}) = \frac{\pi S(\omega_\mathrm{i})}{2T\Delta\omega |\hat{Y}_\mathrm{i}|^2} (u_\mathrm{i}^2 + \bar{u}_\mathrm{i}^2) \qquad \forall \; \frac{|\hat{Y}_i|}{|\hat{Y}_{\max}|} > 0.1 \,. \tag{8}$$

It is important that the formula is only applied to frequencies satisfying the amplitude condition stated at the end of the equation, since small amplitudes lead to instabilities. The value of 0.1 is adapted from Takami et al. [4]. The wave spectral parameters, namely the significant wave height H_s and wave peak period T_p, can be calculated from integral formulations of the spectrum [26].

The wave profile is calculated with the phase angles between wave and motions $\phi_\mathrm{i} = \arg(\hat{Y}(\omega_\mathrm{i}))$ and wave amplitudes calculated from the wave spectrum

$$\zeta(t) = \sum_{i=1}^{n} \frac{\sqrt{S(\omega_\mathrm{i})\Delta\omega}}{|\hat{Y}(\omega_\mathrm{i})|} \Big(u_\mathrm{i} \cos(\omega_\mathrm{i} t - \phi_\mathrm{i}) - \bar{u}_\mathrm{i} \sin(\omega_\mathrm{i} t - \phi_\mathrm{i}) \Big) \qquad \forall \; \frac{|\hat{Y}_i|}{|\hat{Y}_{\max}|} > 0.1 \,. \tag{9}$$

The resulting wave profiles are evaluated using two metrics: one that evaluates the phases (correlation) and one that evaluates the amplitudes (wave spectra difference). The mean correlation $\bar{\gamma}_\zeta$ is calculated similarly to (7), but using two wave profiles ζ_1 and ζ_2

$$\bar{\gamma}_\zeta = \frac{1}{n} \sum_{i=1}^{n} \frac{(\zeta_1(t_\mathrm{i}) - \mu_1) \cdot (\zeta_2(t_\mathrm{i}) - \mu_2)}{\sigma_{1,1} \cdot \sigma_{1,2}} \,. \tag{10}$$

The correlation is independent of the signals amplitude and only evaluates phase differences of the signals. No phase differences between the signals lead to a correlation of 1, whereas opposite phase differences lead to -1. The wave spectra amplitude is evaluated based on the normalized root mean square error (NRMSE)

$$\mathrm{NRMSE} = \frac{\sqrt{\int_0^{\omega_{\max}} (S_{\zeta,1}(\omega) - S_{\zeta,2}(\omega))^2 \, \mathrm{d}\omega}}{\int_0^{\omega_{\max}} S_{\zeta,1}(\omega) \, \mathrm{d}\omega} \,. \tag{11}$$

The difference is normalized with the area of the input wave spectrum $S_{\zeta,1}(\omega)$, which cannot be zero. The NRMSE is computed using the wave spectrum data instead of the time series. Calculating the NRMSE for two time series includes phase and amplitude information. However, to investigate the limits of the methodology it is beneficial to separate both effects. The wave spectrum is independent of the wave phase and enables the evaluation of the results' accuracy separately regarding phase and amplitude.

2.3. Combined PSWF-SL Methodology

In this section, the combined PSWF and SL methodology (PSWF-SL) for improved wave estimation is introduced. The SL approach is included from Section 2.1, whereas the PSWF described in Section 2.2 is adapted to include SL. Figure 1 shows the concept of the combined methodology. In comparison to the PSWF method, the sequential estimation of the PSWF and wave parameters is replaced with an iterative loop including the SL with the RAO as output. The iteration is executed until the change in the SL parameters $K_{\mathrm{eq,ext}}$, $R_{\mathrm{eq,ext}}$ between two consecutive iterations i is smaller than a set boundary of 10^{-5}:

$$\epsilon = |1 - \sqrt{\frac{K^2_{\mathrm{eq,ext,i}} + R^2_{\mathrm{eq,ext,i}}}{K^2_{\mathrm{eq,ext,i-1}} + R^2_{\mathrm{eq,ext,i-1}}}}| < 10^{-5}\,. \tag{12}$$

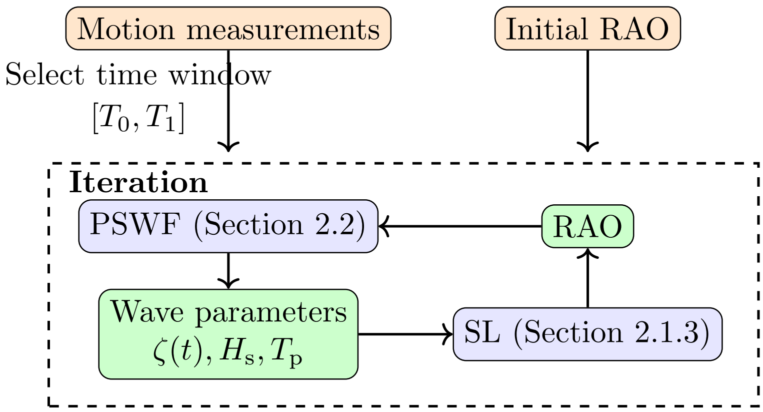

Figure 1. Modular visualization of the combined PSWF-SL methodology. Orange boxes indicate input data, blue boxes indicate the calculation from the previous section, and the green boxes indicate the output parameters in each iteration.

The linearized coefficients applied in the SL calculation are saved after the iteration and used as input for the next iteration. The established method is based on two nested iterations. The following Algorithm 1 lists the calculation steps in the current methodology:

Algorithm 1: PSWF-SL methodology

Input: Measured motion signal $z(t)$, initial RAO $\hat{Y}(\omega)$
Output: Wave profile $\zeta(t)$, Adapted RAO $\hat{Y}^*(\omega)$, Wave parameters H_s, T_p
Set $K_{\mathrm{eq,ext}} = 0$, $R_{\mathrm{eq,ext}} = 0$, $\hat{Y}^*(\omega) = \hat{Y}(\omega)$;
Time window loop: repeat
  PSWF: Reconstruct motion with PSWF (4);
  Calculate wave profile and spectrum with (8) and (9);
  PSWF Iteration: repeat
    SL Iteration: repeat
      Calculate response spectrum $S(\omega) = |\hat{Y}^*(\omega)|^2 S_\zeta(\omega)$;
      Determine SL for each nonlinearity;
      Evaluate new RAO $\hat{Y}^*$ with $K_{\mathrm{eq,ext}}$, $R_{\mathrm{eq,ext}}$;
      Save SL parameters for calculation of ϵ_1;
    until $\epsilon_1 < 10^{-5}$ *from* (12);
    Calculate wave profile and spectrum with (8) and (9);
    Save SL parameters for calculation of ϵ_2;
  until $\epsilon_2 < 10^{-5}$ *from* (12);
until *End of simulation time*;

Combining both iterations into a single optimization problem would introduce a strong bidirectional coupling between wave spectral parameters and the RAO. Since the PSWF-SL output depends on both quantities, the resulting objective function becomes prone to multiple local minima. The nested approach avoids this issue by alternating between wave parameter estimation for a fixed RAO and an SL RAO adaptation based on the updated wave parameters. Developments during this study converged after 5–10 outer iterations.

3. Results and Discussion

To verify the broad applicability of the proposed method to different applications and types of nonlinearities, two geometries are adopted in this work, and the results are inherently structured in five Sections. A floating cylinder with viscous drag is presented in Section 3.1, a sphere subject to nonlinear hydrostatic forces is discussed in Section 3.2, and a sphere subject to viscous drag and nonlinear hydrostatic forces is examined in Section 3.3. Sections 3.4–3.6 contain studies for Gaussian assumption, noisy and multiple DOF motions.

3.1. Floating Cylinder with Viscous Drag

3.1.1. Simulation Setup

A generic cylindrical floater, as shown in Figure 2, is adopted as the first research reference. The floater is restricted to heave motion only, and the mooring tension is modeled as a linear spring force in the vertical direction. The considered nonlinear effect in this case is the viscous drag force. The main geometrical and simulation parameters used in this case are summarized in Table 1.

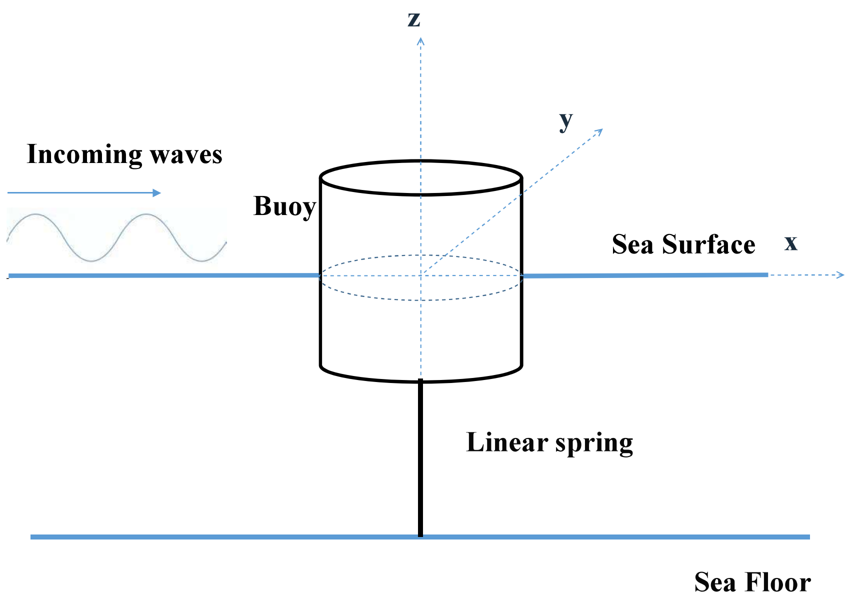

Figure 2. Schematic of the cylindrical floater.

The viscous drag force can be described following Morison equation as

$$F_{\text{vis}} = -\frac{1}{2} C_{\text{d}} \rho A_{\text{s}} v |v| \,, \tag{13}$$

where F_{vis} is the viscous drag force, C_{d} is the drag coefficient, A_{s} is the area of the body projected in the direction of motion, ρ is the water density, and v is the floater velocity. The linearized viscous damping term can be represented in the frequency domain as

$$\hat{F}_{\text{vis}}(\omega) = R_{\text{eq,vis}} \hat{v}(\omega) \,, \tag{14}$$

where $\hat{v}$ is the complex amplitude of the floater velocity, and $R_{\text{eq,vis}}$ is the statistically linearized viscous damping coefficient. The coefficient has been derived in previous studies [15] as

$$R_{\text{eq,vis}} = \frac{1}{2}\rho C_{\text{d}} A_{\text{s}} \sigma_{\text{v}} \sqrt{\frac{8}{\pi}}, \tag{15}$$

where σ_{v} stands for the standard deviation of the floater's velocity. Thus, the equation of motion of the SL approach can be rewritten specifically for this case as

$$\hat{F}_{\text{e}}(\omega) = \hat{z}(\omega)\left\{-\omega^2\left[M + M_{\text{r}}(\omega)\right] + K_{\text{hs}} + K_{\text{mooring}} + \text{i}\omega\left[R_{\text{r}}(\omega) + R_{\text{eq,vis}}\right]\right\}. \tag{16}$$

Simulations are carried out for an array of significant wave heights H_{s} and peak periods T_{p} as listed in Table 2. The selected limits of wave height and period correspond to the most probable worldwide wave conditions following DNVGL-CP-205 [31]. The maximum height is restricted due to the applicability of the RAO in certain cases, which becomes less reliable when wave amplitudes exceed the floater's draft. The simulation time is set to 1000 s with a time step of 0.1 s. Results are only shown for the 900 s simulation time after the initial ramp phase.

Table 1. Simulation parameters of the cylindrical floater moving in one DOF (heave) or three DOFs (surge, heave, and pitch).

Parameters	Quantities
Radius R	5 m
Height	10 m
Mass M	402,520 kg
Center of gravity	$(0, 0, -1.5)$ m
Floater draft	5 m
Water depth	100 m
1 DOF Drag coefficient C_{d}	1
3 DOF Drag coefficient C_{d}	$\text{diag}(1, 1, 1)$
1 DOF Mooring stiffness	$20\,\frac{\text{kN}}{\text{m}}$
3 DOF Mooring stiffness	$\text{diag}(20\,\frac{\text{kN}}{\text{m}}, 20\,\frac{\text{kN}}{\text{m}}, 500\,\frac{\text{kN}}{\text{m rad}})$
Water density ρ	$1025\,\frac{\text{kg}}{\text{m}^3}$

Table 2. Wave spectral parameter ranges for motion calculations.

Parameter	Min	Max	Step
Significant wave height H_{s} [m]	1	5	0.5
Peak wave period T_{p} [s]	5	15	1

3.1.2. Convergence Studies

The PSWF-SL methodology is dependent on the accuracy of the RAO and a suitable approximation of the nonlinear effects with SL. Variables influencing the accuracy are the time window size $2T$ and the iteration boundary ϵ from (12).

Figure 3 demonstrates that selecting time windows of 240 s (4 min) as described in Section 2.2 led to high correlation and low NRMSE values. Reducing the time window size down to 30 s led to higher deviations in the resulting wave profiles, especially in high amplitude waves. Deviations are attributed to the assumed Gaussian distribution, which is violated when only a small number of peak wave periods (approximately three in the case of 30 s window size) are captured within a time window.

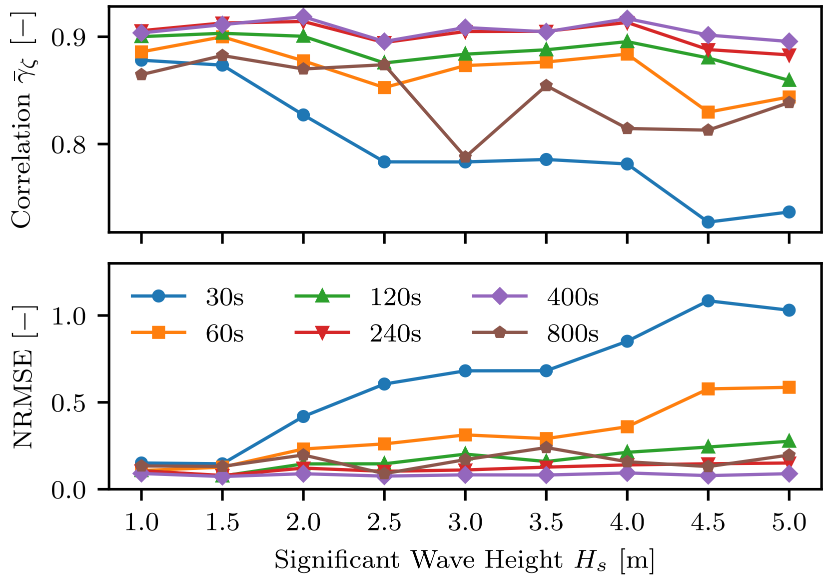

Figure 3. Correlation and NRMSE of PSWF-SL methodology with various time window sizes $2T$ for cylinder in waves with 10 s peak period plotted over wave height.

Figure 4 shows the convergence of the correlation, NRMSE, and the factor between CPU and simulated time. The simulation were executed on a single core of a standard desktop PC with an Intel i7-8700 CPU with 3.2 GHz. A convergence limit ϵ of 10^{-5} results in high accuracy with low computational effort. Decreasing the limit reduces the number of inner and outer iterations as described in Section 2.3, which had no measurable influence calculation time in this study. The convergence limit of $\epsilon = 0.5$ results in a single iteration, which demonstrates that a single loop in Figure 1 and Algorithm 1 led to acceptable accuracy.

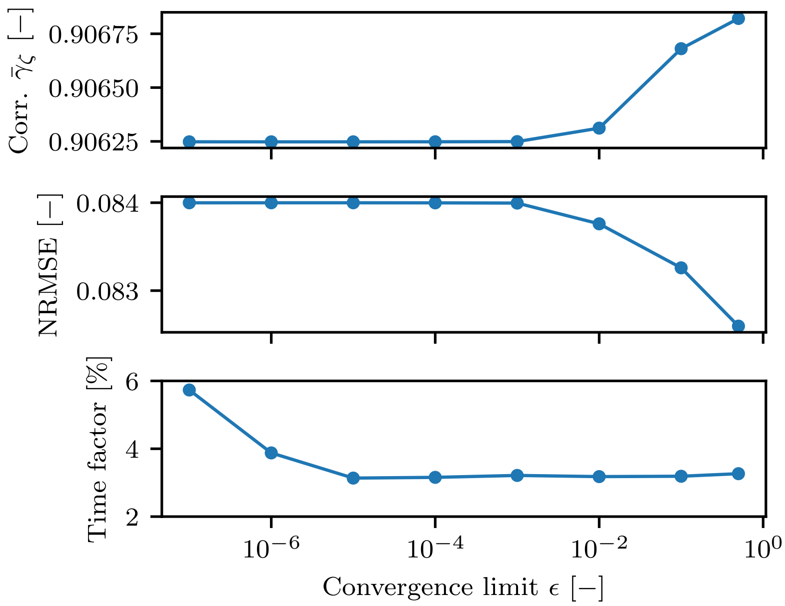

Figure 4. Convergence study of the iteration limit ϵ from (12). Correlation, NRMSE, and time factor between CPU and estimation time for the cylinder in waves with 10 s peak period are averaged for all wave heights.

3.1.3. Comparison of RAOs and Response Spectra

In this section, the response spectra calculated using the Cummins equation, SL, and FD are compared. Figure 5 shows the response spectra for a significant wave height of 3 m and a peak period of 8 s. It shows that the adaptation of the SL significantly reduces the differences in the TD calculations. The spectrum for the TD results is calculated with Welch's method, whereas the spectral and FD spectra are calculated in the frequency domain [26] with

$$S(\omega) = |\hat{Y}(\omega)|^2 S_\zeta(\omega)\,. \tag{17}$$

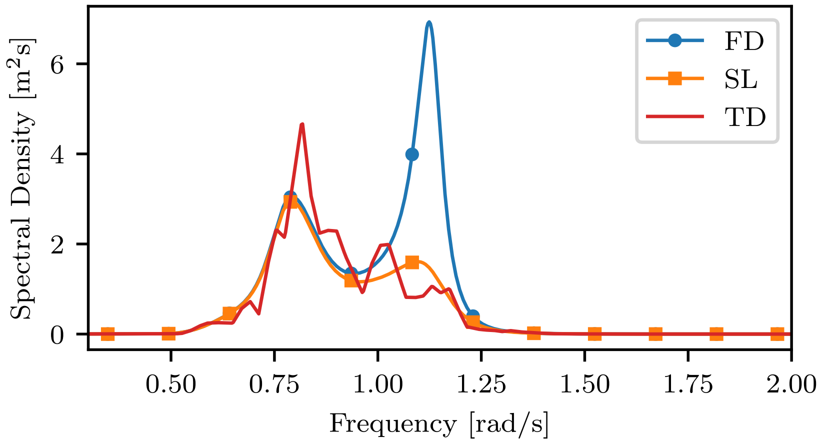

Figure 5. Cylinder response spectra of FD, SL, and TD calculation in waves with significant wave height $H_\mathrm{s} = 3\,\mathrm{m}$ and peak period $T_\mathrm{p} = 8\,\mathrm{s}$.

The peak reduction from FD to SL in Figure 5 can be traced back to the resonance peak of the RAOs shown in Figure 6. The viscous drag correction from (15) inserted into (16) reduces the peak significantly. The RAO phase is only slightly influenced by the SL. This can be explained by the fact that the SL incorporates a correction coefficient related to the motion responses into the equation of motion, which covers viscous drag effects as a damping term.

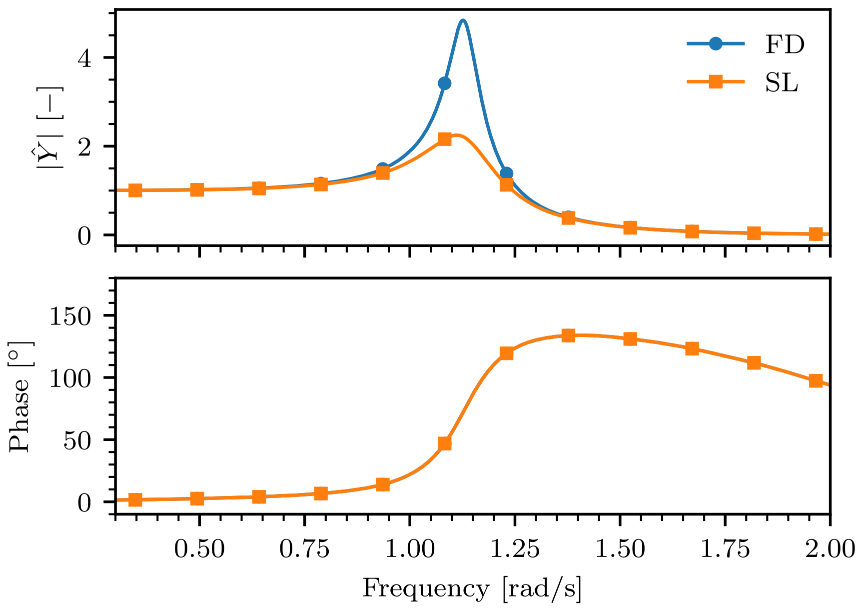

Figure 6. Resulting linear and spectral RAO absolute value and phase for cylinder with viscous drag and in waves with significant wave height $H_\mathrm{s} = 3\,\mathrm{m}$ and peak period $T_\mathrm{p} = 8\,\mathrm{s}$.

3.1.4. Wave Estimations with FD and SL RAOs

In this section, the wave estimations from the PSWF method are compared for FD and SL RAOs as input.

Figure 7 shows the resulting wave profiles for the 50 s of simulation time. The applied RAO are equal to those in Figure 6, which explains the higher wave amplitudes of the SL estimation due to the lower RAO amplitude.

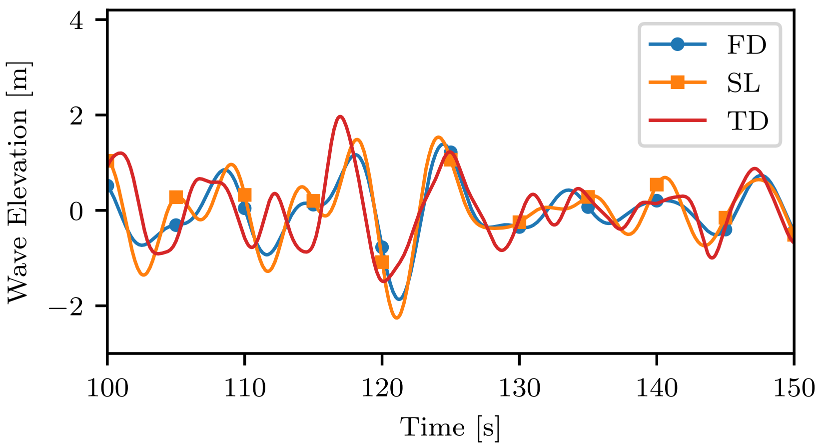

Figure 7. Cylinder calculated and estimated wave profiles with viscous drag in waves with significant wave height $H_s = 3$ m and peak period $T_p = 9$ s with FD and SL RAO.

Figure 8 shows that the qualitative observation from Figure 7 translates into the wave spectra calculated with Welch's method, where the difference between TD and SL is smaller than that between TD and FD. Although the wave energy around the resonance frequency is comparably small relative to the peak wave energy, results show that the adaptation of the RAO can increase the estimation accuracy.

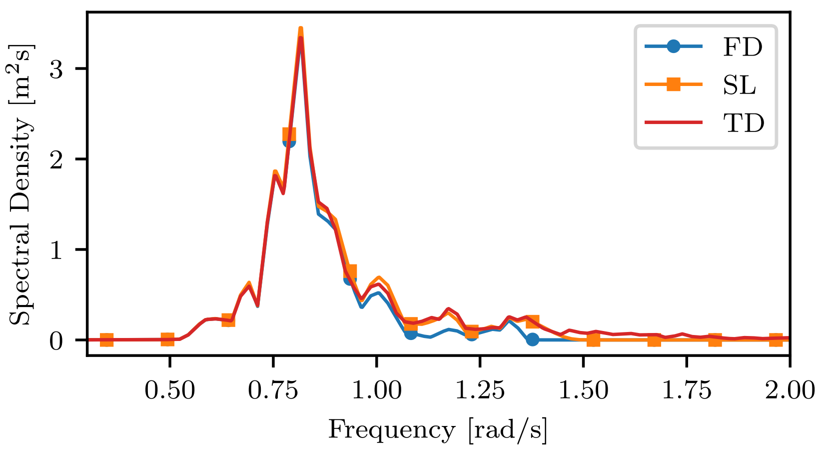

Figure 8. Cylinder wave spectra calculated for wave profiles in Figure 7 with Welch's method. Spectra are calculated for the total simulation time of 900 s.

Figure 9 shows the correlation $\bar{\gamma}_\zeta$ calculated from (10) and the response spectra differences from (11) for the full array of wave height and period combinations in Table 2. The correlation increases in long waves, where the response spectra differences become smaller. Differences between SL and FD are present for small peak periods, where the FD results underestimate the wave spectrum area, as already shown in Figure 8 for a peak period of 8 s. At very low wave peak periods ($T_p < 6$ s), small motion amplitudes of the cylinder hinder accurate wave estimation since the PSWF method only includes amplitudes greater than 10% of the maximal value of the RAOs, as shown in (9). The dashed lines indicate the correlation and NRMSE of the 5 m wave height results and show that the viscous drag has a nonlinear influence on the wave spectra shape in Figure 9, but not on the phase components. SL can adapt the RAO amplitude, resulting in significantly lower deviations overall and between multiple wave heights for a fixed period.

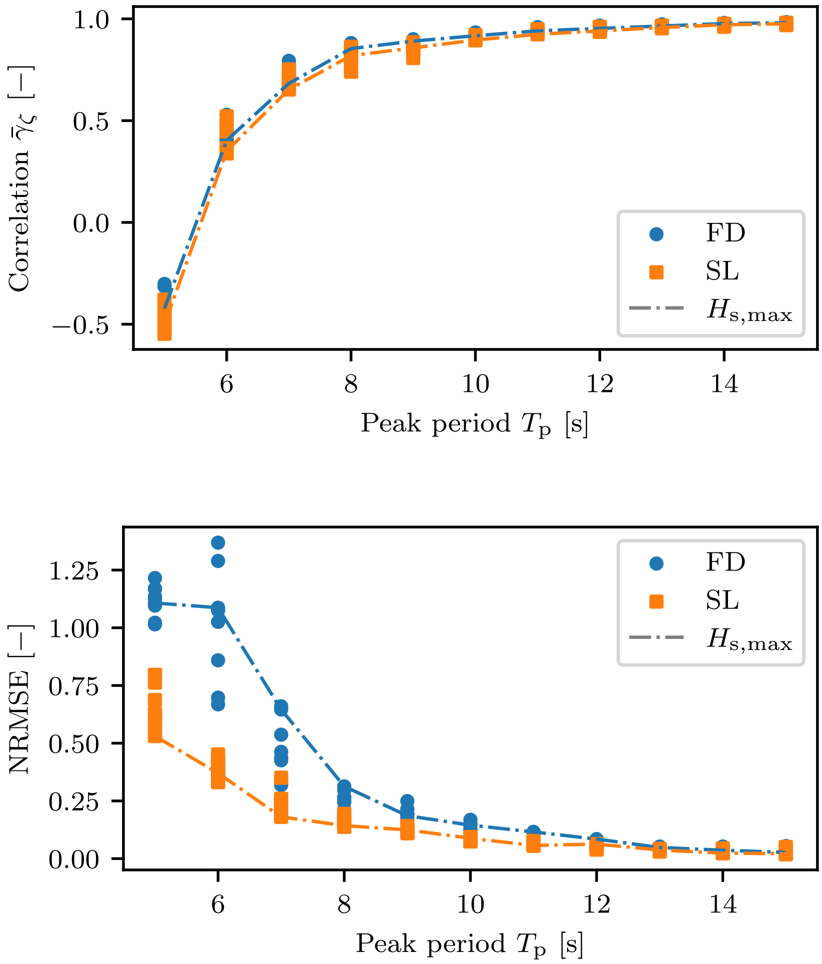

Figure 9. Correlation and NRMSE of FD and SL cylinder wave estimations plotted over peak period. Dashed line indicates the point with highest significant wave height.

3.1.5. Wave Estimations with PSWF-SL Methodology

In this section, the wave estimations from the PSWF method with RAOs derived from the FD modeling as input and the combined PSWF-SL method are compared.

Figure 10 repeats the results from FD, but they are compared to the developed PSWF-SL methodology. Similar to Figure 9, the combined methodology performs better for the NRMSE, but it is associated with slightly reduced accuracy for the correlation. The application of the PSWF-SL methodology is successful and demonstrates that the adaptation of the RAO in each time window is possible, resulting in similar accuracy to that of applying SL after all measurements are gathered. It is important to highlight that the SL method is not suitable for onboard application since it can only be applied after measuring the motions. PSWF-SL can be applied during measurements and does not increase the evaluation time as shown in Figure 4. The results of SL in Figure 9 compared to PSWF-SL in Figure 10 show approximately the same correlations and NRMSE values. This proves that the PSWF-SL methodology is able to identify the best fitting RAO with a short time window as input. Compared to the PSWF results from Wermbter et al. [7], this is advantageous as the required database can be much smaller when certain parameters are known, e.g., the drag coefficient.

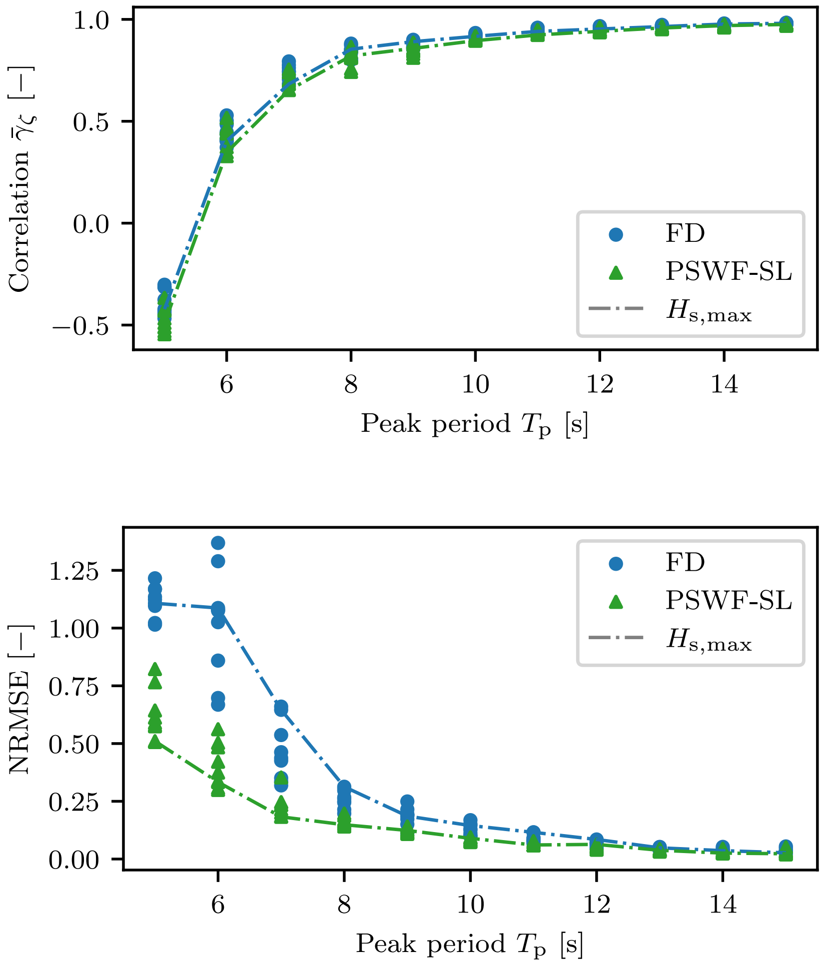

Figure 10. Correlation and NRMSE of FD and PSWF-SL cylinder wave estimations plotted over peak period. Dashed line indicates the point with highest significant wave height.

One of the key features of the PSWF-SL method is that it can adapt to instantaneous changes in the wave conditions and the dynamic behavior of the floater. Figure 11 shows that the significant wave height varies significantly during 900 s of measurements. Assuming nonlinearity of motions, as already shown in Figures 9 and 10, the PSWF-SL method allows for unique RAO adaptations depending on the current significant wave height.

Figure 12 shows that the PSWF-SL method is able to adapt the RAO for each time window successfully and reduce the NRMSE compared to the SL and FD methods for all wave height bins. Standard deviations remain constant compared to the mean values of NRMSE. Bins with a width of 20% difference to the mean wave height were selected, because this value corresponds to a 0.2 m change in 1 m mean wave height and 1 m in 5 m mean wave height. These changes should lead to noticeable changes in motion amplitudes. The advantage of PSWF-SL compared to FD is greater for higher wave heights, since nonlinear effects have more influence in steeper waves.

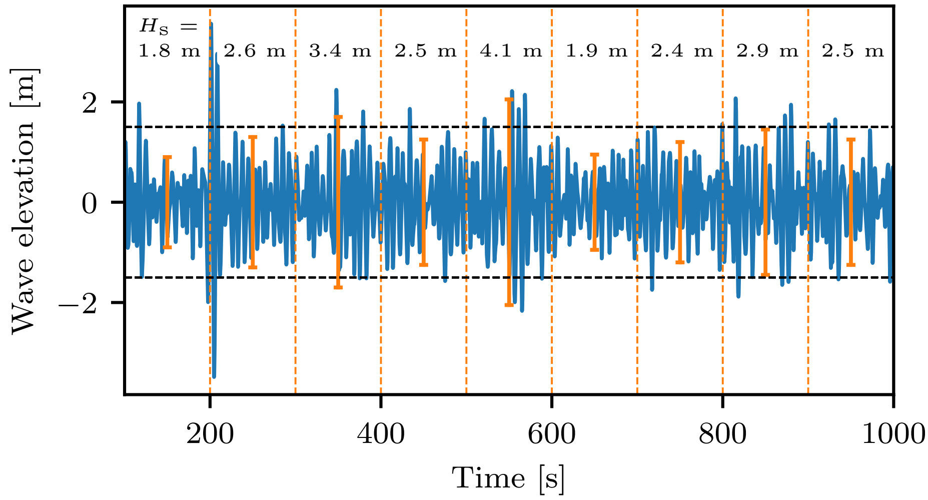

Figure 11. TD-calculated wave profile time series wave with bars each 100 s indicating the significant wave height for each time window. Peak period is 8 s, and mean significant wave height is 3 m; minimum and maximum time window wave heights are labeled.

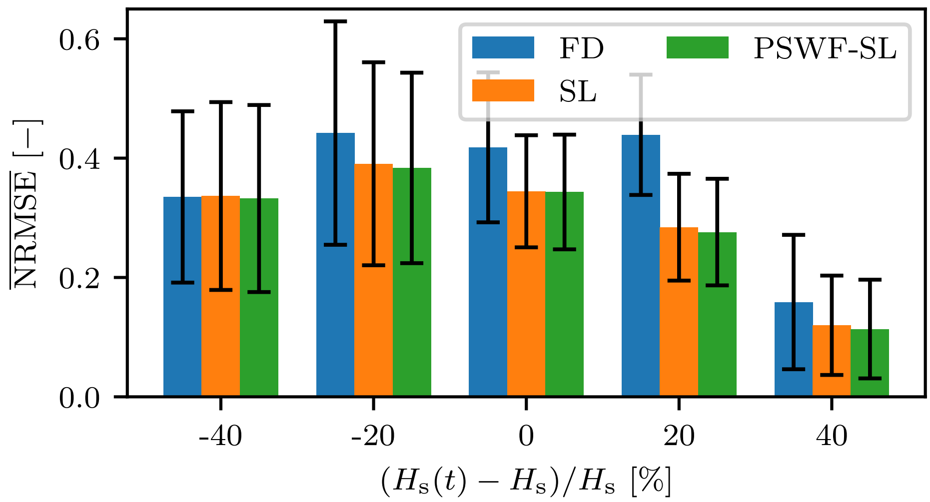

Figure 12. Cylinder mean NRMSE ($\overline{\text{NRMSE}} = \frac{1}{N}\sum \text{NRMSE}_i \,\forall\, H_s(t) \in [0.9H_{s,b}, 1.1H_{s,b}]$, where $H_{s,b}$ is the wave height at the bin center.) and standard deviations indicated by error bars of all time windows and methods sorted into bins characterized by the percentage difference to the mean significant wave height.

3.2. Floating Sphere with Nonlinear Hydrostatic Forces

3.2.1. Simulation Setup

The second case study adopts a floating sphere to specifically investigate the effect of nonlinear hydrostatic forces on the predictive performance of the proposed combined method. The floating sphere is shown in Figure 13, and the relevant simulation parameters are provided in Table 3.

The nonlinear hydrostatic force for the sphere can be expressed as

$$F_{hs}(z) = \rho g V_{sub}(z) - Mg\,, \tag{18}$$

where V_{sub} is the instantaneous submerged volume of the sphere. As detailed in [21], the statistically linearized representation to (18) can be derived as follows:

$$K_{\text{eq,hs}} = \pi\rho g(\sigma_z^2 - 2dR + d^2)\,, \tag{19}$$

where σ_z, d, and R embody the standard deviation of the displacement and the floater's draft and radius. Subsequently, the equation of motion for the sphere can be given as

$$\hat{F}_e(\omega) = \hat{z}(\omega)\left\{-\omega^2\Big[M + M_r(\omega)\Big] + K_{\text{eq,hs}} + K_{\text{mooring}} + i\omega R_r(\omega)\right\}. \tag{20}$$

The simulated wave heights and periods are according to the previous investigations on the cylinder and are listed in Table 2.

Table 3. Simulation parameters of the spherical floater.

Parameters	**Quantities**
Radius R	5 m
Mass M	268,208 kg
Projected area A_s	78.5 m^2
Floater draft	5 m
Water depth	100 m
Water density ρ	1025 $\frac{\text{kg}}{\text{m}^3}$
Mooring stiffness K_{mooring}	20 $\frac{\text{kN}}{\text{m}}$

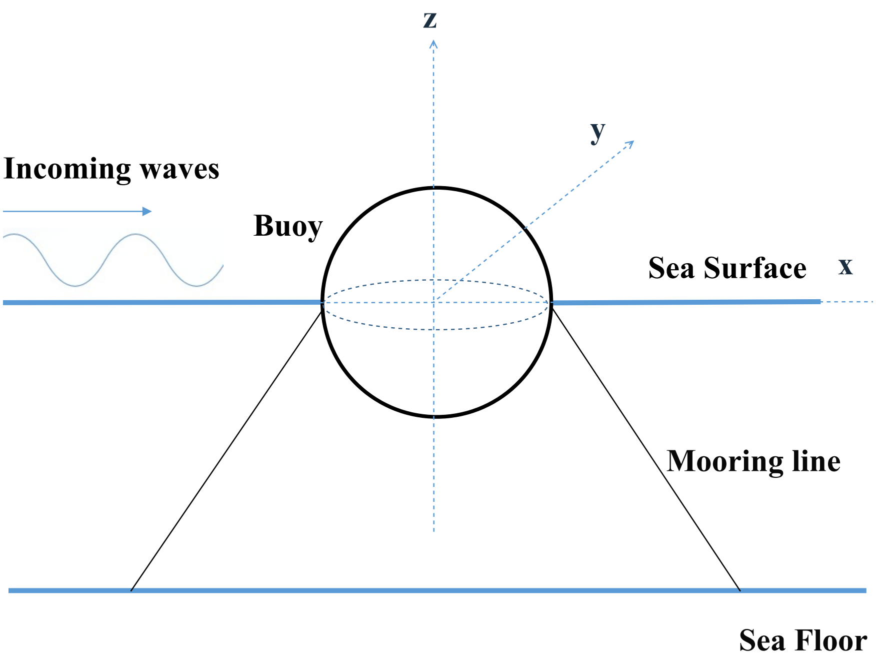

Figure 13. Schematic of the spherical floater.

3.2.2. Wave Estimations with the Linear FD and SL Approaches

In this section, the wave estimations obtained using the PSWF method with RAOs acquired from the FD and SL approaches are compared for the spherical floater, considering nonlinear hydrostatic effects.

Figure 14 shows the resulting RAOs from SL and FD. In comparison to Figure 6, the modeling of nonlinear hydrostatics leads to a slight amplitude increase and, more importantly, to a shift in the resonance frequency.

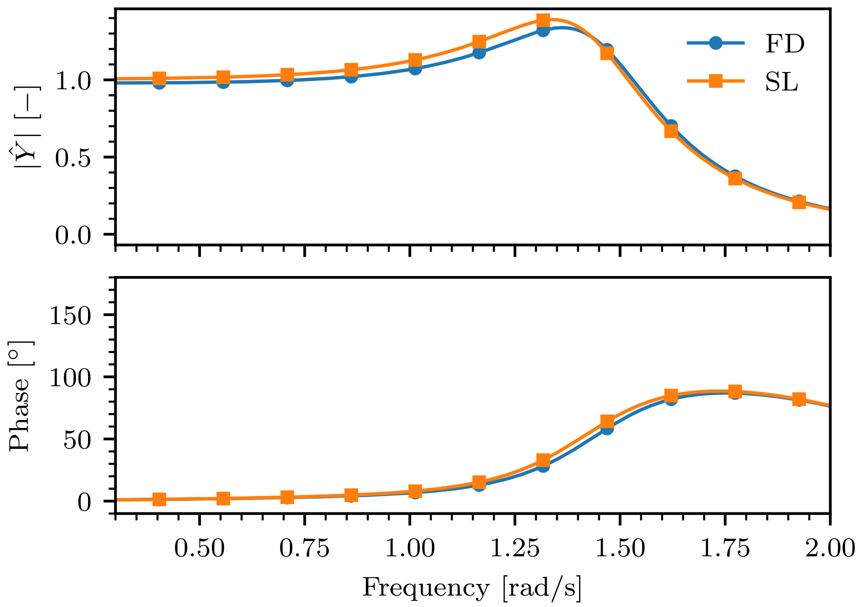

Figure 14. Resulting linear and spectral RAO absolute value and phase for sphere with nonlinear hydrostatic forces and in waves with significant wave height $H_s = 3$ m and peak period $T_p = 8$ s.

The comparison of the FD and SL methods on the estimated results' correlation and NRMSE over the peak period in Figure 15 shows that nonlinear hydrostatics have a stronger influence on the wave estimations than the viscous drag. The NRMSE values are higher, especially for periods between 6 and 8 s. The SL RAO strictly reduces the NRMSE by at least 50%. The wave height has a strong influence on the results, and it may be concluded that the nonlinear hydrostatics introduced by varying the submergence of the sphere can be represented by a motion amplitude-dependent term in (19), whose value changes with each wave condition. However, the submergence of the sphere depends on hydrostatics and wave forces. Representing the hydrostatics with a motion dependent term introduces an error due to the smearing of the wave and hydrostatic forces. It should be replaced with a term depending on the relative vector between the water surface and the sphere's center of gravity. The resonance amplitude in Figure 14 corresponds to a period around 5 s, implying that the investigated wave conditions are mainly in the regime where relative motions between the sphere and the wave elevation are small. The investigation of sub-resonance periods will be addressed in future work.

3.2.3. Wave Estimations with PSWF-SL Methodology

In this section, the wave estimations from the PSWF method with FD RAOs and the PSWF-SL method are compared for the sphere with nonlinear hydrostatics.

Comparing the results generated with FD and PSWF-SL in Figure 16 shows that the PSWF-SL correlation is higher, and the NRMSE is strictly lower than the FD results. PSWF-SL replicates the SL results from the previous section apart from the highest wave height, where the NRMSE is higher; however, the correlation is also higher. As discussed in the previous section, the uncertainty regarding the separation of wave and hydrostatic forces is not straightforward, especially for PSWF-SL, as the short time windows introduce more uncertainty, since it cannot be assumed that the motions and waves follow a Gaussian distribution.

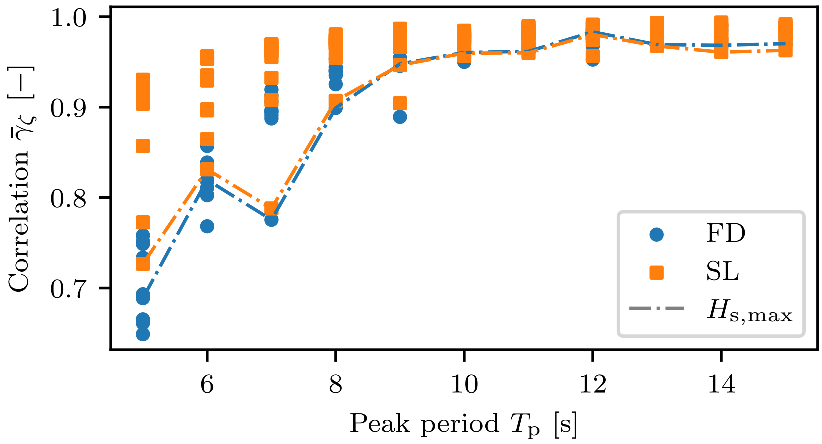

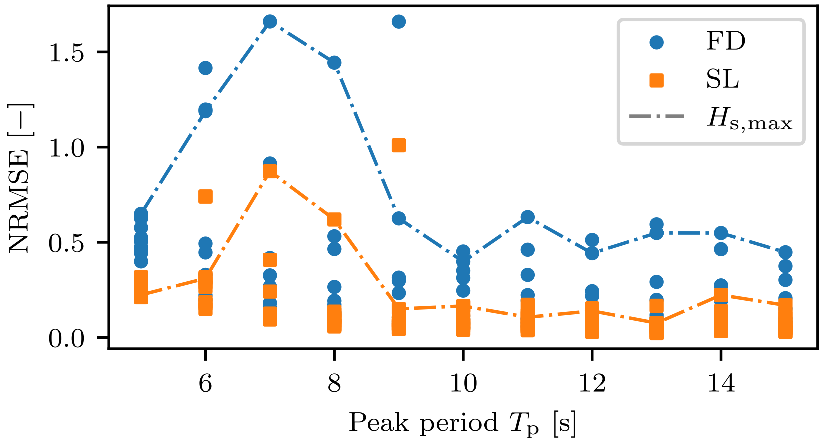

Figure 15. Correlation and NRMSE of FD and SL sphere wave estimations plotted over peak period. Dashed line indicates the point with the highest significant wave height.

Figure 17 summarizes the findings from Figures 15 and 16, showing that with higher wave heights, the FD results perform worse while the SL and PSWF-SL methods perform better. PSWF-SL is slightly worse than SL due to the fact that the instantaneous change during the short time windows may violate the statistical assumptions described in Appendix A. Therefore, an adaptation of the assumed Gaussian distribution to the measured motion-amplitude distribution may be considered in future work.

3.3. Floating Sphere with Nonlinear Hydrostatic Forces and Viscous Drag

In this section, the wave estimations from the PSWF method with RAOs derived from linear FD modeling and the proposed PSWF-SL method are compared for the sphere with nonlinear hydrostatics and viscous drag.

Figure 18 shows that the correlation with PSWF-SL is above 0.9 for almost all cases, and the RMSE is below 0.2. The reported accuracy is higher than the accuracy when only nonlinear hydrostatics were applied in the previous section. FD and PSWF-SL are not as sensitive to wave height when comparing with the results in Figure 16. Viscous drag reduces the motion amplitudes and improves the performance of the PSWF method. Less variation in motion amplitudes is beneficial since small errors in the predicted amplitudes and phases do not lead to strong variations in the resulting wave profile.

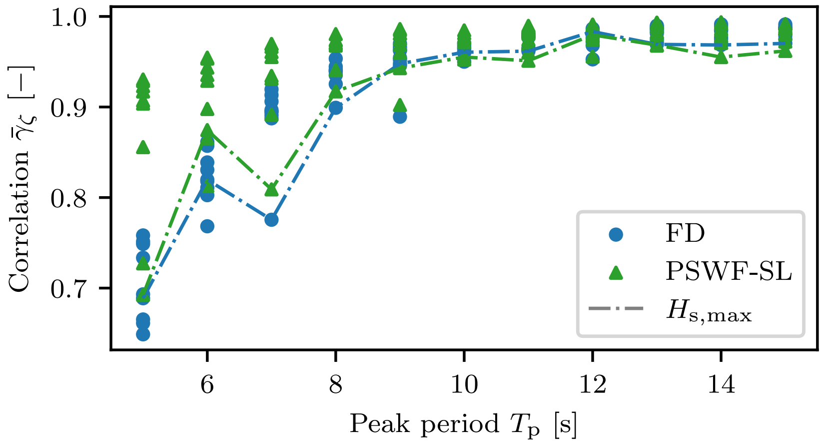

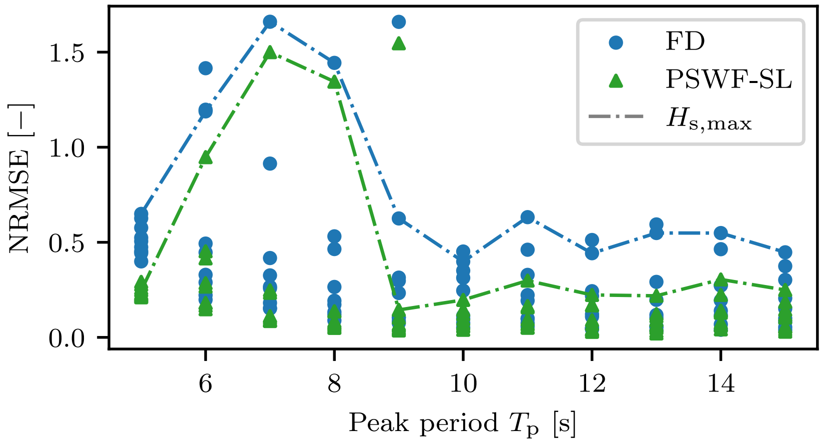

Figure 16. Correlation and NRMSE of FD and PSWF-SL sphere wave estimations plotted over peak period. Dashed line indicates the point with highest significant wave height.

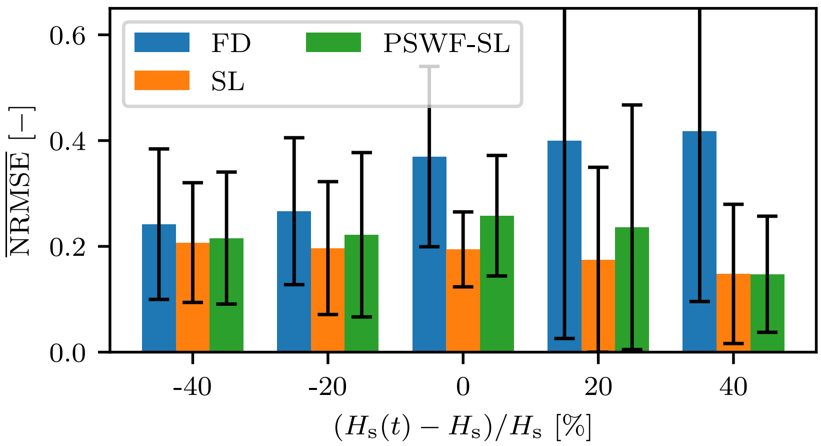

Figure 17. Sphere mean NRMSE ($\overline{\text{NRMSE}} = \frac{1}{N}\sum \text{NRMSE}_i \, \forall \, H_s(t) \in [0.9H_{s,b}, 1.1H_{s,b}]$, where $H_{s,b}$ is the wave height at the bin center) and standard deviations indicated by error bars of all time windows and methods sorted into bins characterized by the percentage difference to the mean significant wave height.

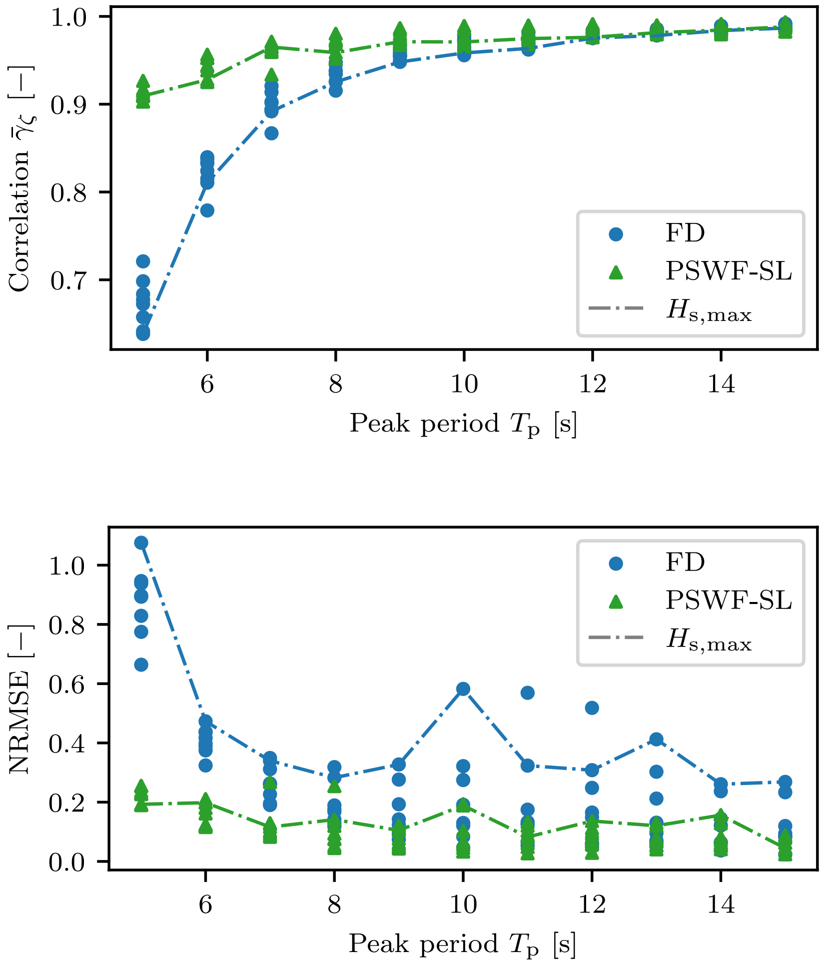

Figure 18. Correlation and NRMSE of FD and PSWF-SL sphere wave estimations with nonlinear hydrostatics and viscous drag plotted over peak period. Dashed line indicates the point with highest significant wave height.

Figure 19 summarizes the results from nonlinear hydrostatics and viscous drag computation and shows an almost linear reduction of deviations for increasing wave height for PSWF-SL. The FD NRMSE is not increasing as strongly as when applying both nonlinear hydrostatics and viscous drag. The effects counteract each other, being beneficial for PSWF estimation. Standard deviations of FD are greater for the wave height outliers indicating that these cases are strongly influenced by nonlinearities. Standard deviations of PSWF-SL remain approximately constant relative to the mean NRMSE.

In real-world conditions, floating structures are exposed to multiple nonlinear effects, measurement bias, and noise, which is investigated in the next Section 3.4. Extending to multiple DOFs is investigated in Section 3.6, which was introduced by Takami et al. [4] and strengthens the stability and applicability of the PSWF algorithm. Although the current results are limited to Cummins equation results, they demonstrate the method's capabilities, given that the Cummins equation accurately represents hydrostatics and viscous drag [32,33].

3.4. Influence of Gaussian Distribution Assumption

Assuming a Gaussian distribution of the floater response allows, from a practical perspective, the derivation of equivalent linearized coefficients in the SL procedure when the underlying system dynamics are unknown. This assumption remains well justified in ocean engineering applications characterized by linear wave regimes. However, several factors may challenge its validity. In addition to the increased nonlinearity discussed in Section 2.1 and Appendix A, the combination of PSWF and SL applied over short time windows may also violate this assumption. To investigate the difference between the assumption and the measured distribution, the mean values in (A6) are evaluated for each time window. Calculating the mean values increases the computational effort only slightly. The results presented in this section are for the sphere with hydrostatic drag, because the deviations were the greatest among the investigated cases.

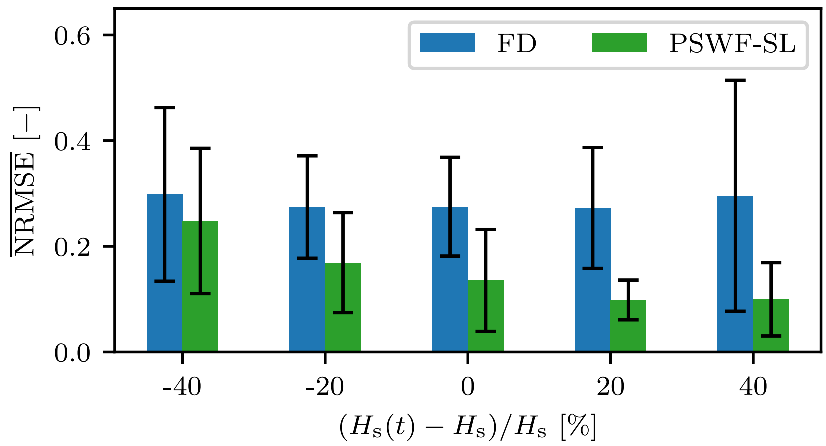

Figure 19. Sphere mean NRMSE ($\overline{\mathrm{NRMSE}} = \frac{1}{N}\sum \mathrm{NRMSE_i}\ \forall\, H_s(t) \in [0.9H_{s,b}, 1.1H_{s,b}]$, where $H_{s,b}$ is the wave height at the bin center) and standard deviations indicated by error bars with nonlinear hydrostatics and viscous drag of all time windows and methods sorted into bins characterized by the percentage difference to the mean significant wave height.

Figure 20 shows the NRMSE between each time window and the Gaussian distribution calculated from the mean and standard deviation of the time windows. Higher wave heights increase the deviations and scatter among the results. These deviations originate from the measured wave elevation distribution and the nonlinear contribution of hydrostatic forces, which increase deviations due to nonlinear transformation of the wave elevation into heave motions.

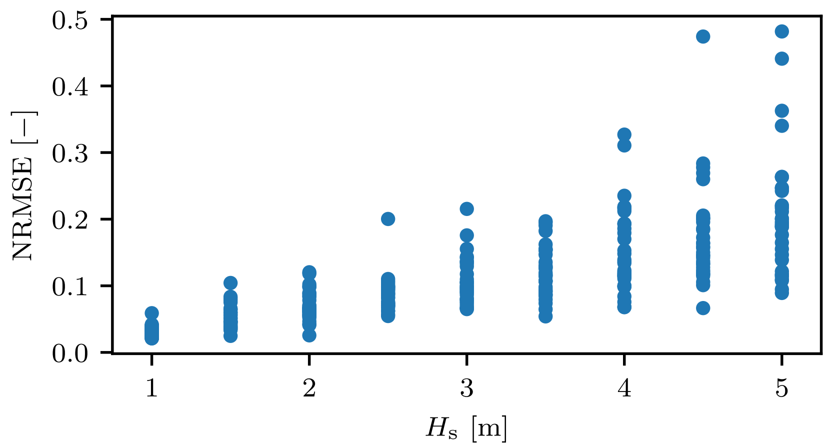

Figure 20. NRMSE between the measured heave displacement distribution and the normal distribution of every time window. Results are shown for the sphere with nonlinear hydrostatics and are plotted over wave height.

Figure 21 shows the distributions for the maximal NRMSE deviation in Figure 20. The measured distribution shows a higher kurtosis compared to the Gaussian distribution. Although, the NRMSE value is around 0.5, the shown deviations are expected to be acceptable when applying the Gaussian distribution formulae, because the resulting SL formula for distributions varying only in kurtosis are going to differ by a small factor.

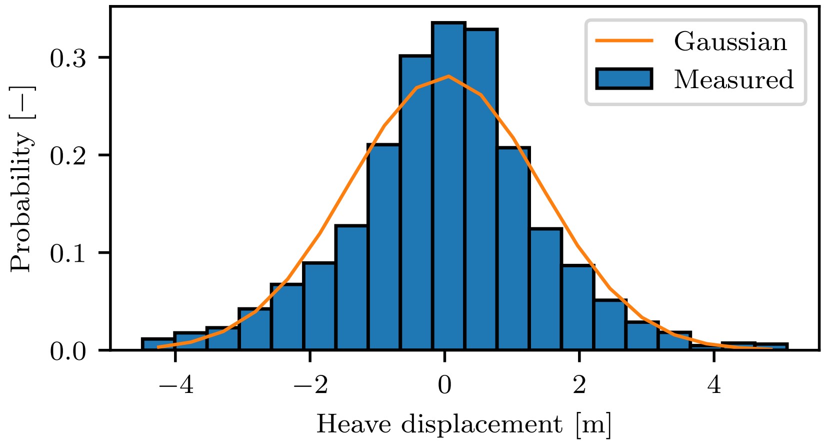

Figure 21. Histogram and Gaussian distribution for waves of height $H_s = 5\,\mathrm{m}$ and period $T_p = 9\,\mathrm{s}$ corresponding to the maximal deviation in Figure 20.

Figure 22 compares correlation and PSD for PSWF-SL with the Gaussian formulae and the evaluation of (A6). Correlations increase for all calculated wave conditions, whereas the PSD values are only partly improved. The red circles indicate the maximal deviating wave condition shown in Figure 21. Although, the distributions were initially deviating strongest, the resulting correlation and PSD are not the highest, which indicates that the Gaussian assumption is not strongly violated.

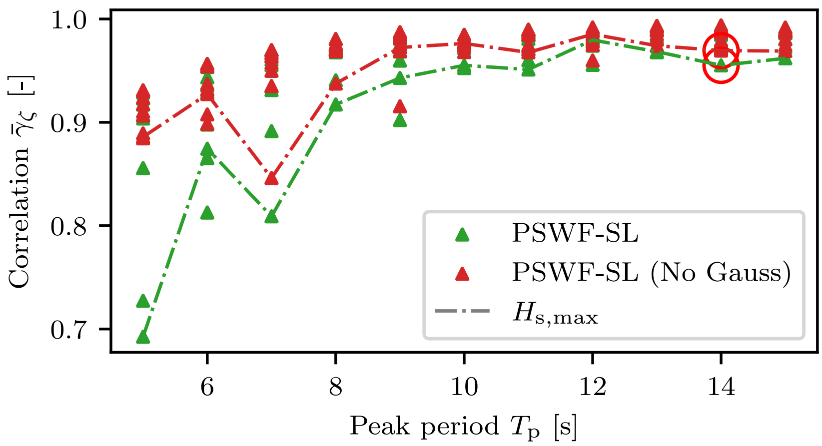

Figure 22. *Cont.*

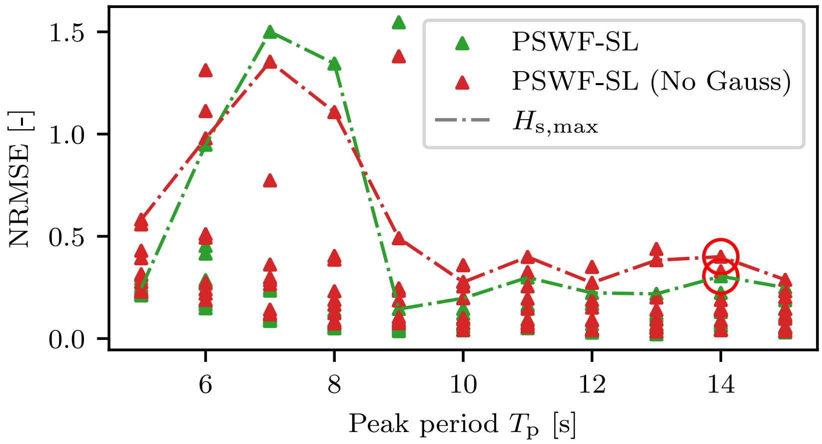

Figure 22. Correlation and NRMSE of PSWF-SL and PSWF-SL with noise and drift for sphere wave estimations with nonlinear hydrostatics plotted over peak period. Dashed line indicates the point with highest significant wave height. Circles indicate the correlation and NRMSE of the strongest deviation distribution from Figure 21.

3.5. Influence of Measurement Noise

Real-world measurement data is subject to noise and drift arising from inertial measurement units (IMUs) that measure accelerations and angular velocities. To bridge the gap between numerical simulation and measurement data, Figure 23 presents a time series with artificially introduced noise and drift. The drift is linearly increasing during the simulation time with a value of $d = 0.001\,\frac{\mathrm{m}}{\mathrm{s}}$ corresponding to 1 m at the end of the simulation. The noise $n(t)$ is normally distributed with a standard deviation of $\sigma = 0.3\,\mathrm{m}$ and a mean value $\mu = 0$

$$z_{n+d}(t) = z(t) \cdot n(t) + t \cdot d\,. \tag{21}$$

Figure 24 shows the results of the PSWF-SL methodology with added noise and drift. The correlation is decreasing and the NRMSE value are increasing for the noise and drift data set. In comparison to the previous figures, the minimal, instead of the maximal, wave height of 1 m is connected with a line. The values at low wave heights suffer in accuracy due to the noise, which has a standard deviation almost as big as the wave amplitude and therefore is approximately equal to the heave amplitude as shown in the RAOs in Figure 6. The PSWF algorithm cannot differentiate between noise and the real heave motion, which limits the applicability in low-wave-height cases. Preprocessing of the signal is recommended to remove most of the noise and drift. Further deviations from Cummins equation-based time series may originate from unmodeled dynamics. It has been shown in a previous study with the PSWF methodology [7] that Cummins equation data resulted in comparable accuracy to full-scale measurement data. Future work should include generalizing the RAO identification from a database and including multiple nonlinearities with the combined PSWF-SL methodology on full-scale data.

3.6. Floating Cylinder with Viscous Drag and Surge, Heave and Pitch Motions

As mentioned in Section 3.3, the PSWF methodology benefits from including multiple DOFs, since the evaluation of (9) is possible in a greater frequency range. In this section the floater is calculated with surge, heave, and pitch motions. The drag coefficients are 1 for each DOF, an additional mooring stiffness is introduced for each DOF to prevent drifting. The evaluation of the wave profile follows formulae given in Takami et al. [4,34].

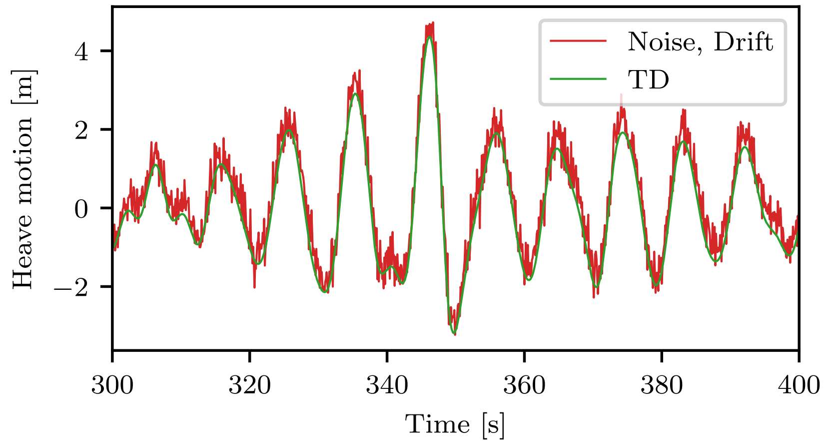

Figure 23. Heave motion and heave motion added with 0.3 m noise and 0.001 $\frac{\mathrm{m}}{\mathrm{s}}$ drift for the motions in waves with a wave height of $H_\mathrm{s} = 3\,\mathrm{m}$ and a peak period of $T_\mathrm{p} = 10\,\mathrm{s}$.

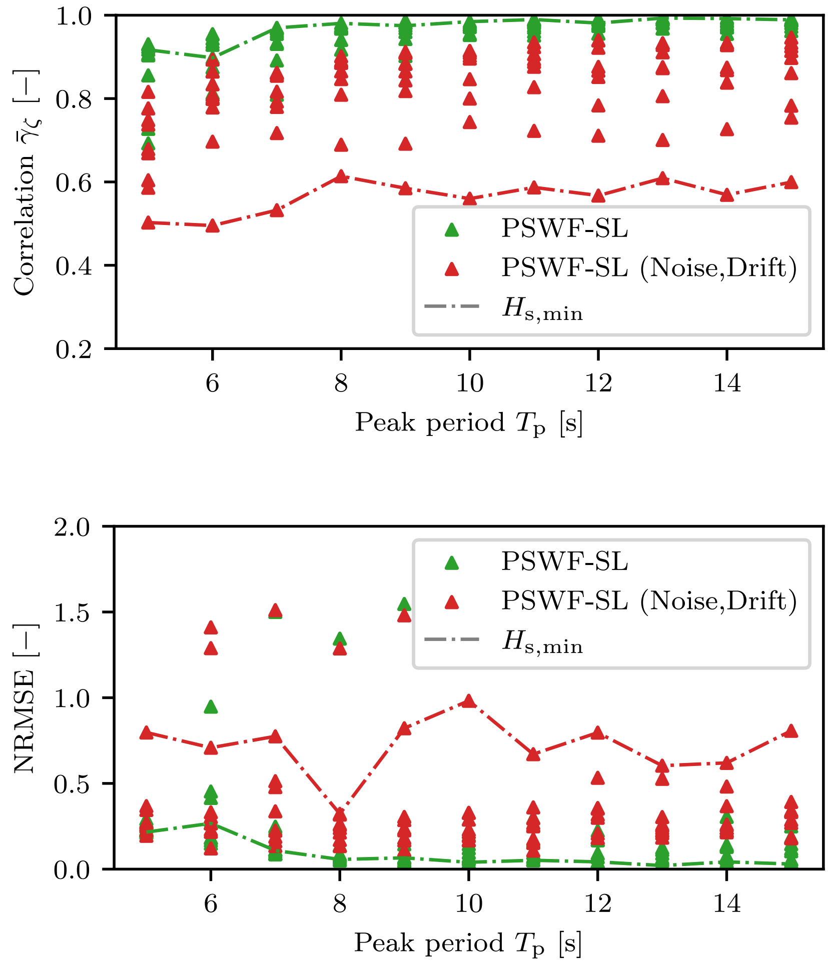

Figure 24. Correlation and NRMSE of PSWF-SL and PSWF-SL without the Gaussian assumption for sphere wave estimations with nonlinear hydrostatics plotted over peak period. Dashed line indicates the point with lowest significant wave height.

Figure 25 shows the correlation and NRMSE for the multiple DOFs calculation. The correlation is higher than for the heaving cylinder in Figure 10, whereas the NRMSE is comparable in waves with periods below 12 s, but increases in periods with periods above 12 s. These deviations occur due to the influence of the mooring system on the surge and pitch motions. In long waves, the cylinder starts to oscillate in surge, heave, and pitch with a frequency equal to the wave frequency, but the amplitude is decreased by the mooring restoring force or moment. The stiffness is included in the RAO, but the system oscillates at eigen frequency and not wave frequency, especially for surge, and therefore the waves are slightly overestimated by PSWF-SL. Including a PSWF-SL formula for mooring could improve the solution, although PSWF-SL with viscous drag damping is already performing slightly better than FD.

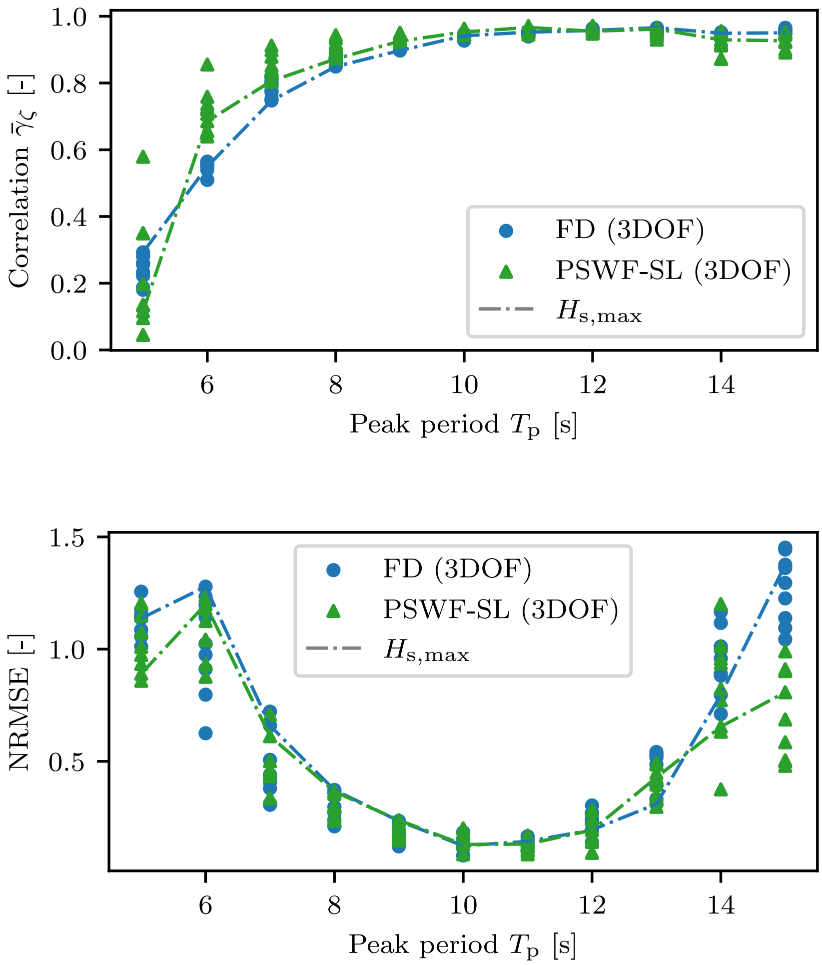

Figure 25. Correlation and NRMSE of FD and PSWF-SL with multiple DOF cylinder wave estimations with viscous drag plotted over peak period. Dashed line indicates the point with highest significant wave height.

4. Conclusions

This study introduces a methodology combining wave estimation with prolate spheroidal wave functions and statistical linearization, aiming for improved wave estimation accuracy. The methodology is based on an iteration of the two individual algorithms returning the RAO and the wave parameters until convergence. The methodology is verified with heave motions from a TD method based on the Cummins equation. A cylindrical floater with quadratic viscous drag and a sphere with nonlinear hydrostatic forces were tested separately to investigate the influence of the nonlinearities. The results led to the following conclusions:

- Calculating a RAO with statistical linearization and applying it in the PSWF wave estimation led to a reduction in spectral differences and higher correlations compared to the linear RAO derived from a potential theory program. Differences in viscous drag calculations were mainly visible in the spectral differences, whereas nonlinear hydrostatics also showed differences in correlation.

- The combined methodology yielded an accuracy comparable to that of RAOs derived using the entire measurement time. Variations in wave height had a limited effect on viscous drag; however, for high wave heights, the accuracy of wave spectra accounting for nonlinear hydrostatic forces was significantly improved by the combined methodology.
- The combined methodology reduced the spectral differences for time windows with higher wave heights more significantly than for lower wave heights. The nonlinear contribution of the hydrostatic forces can be included in wave estimations with the combined methodology.
- Combining both nonlinearities for the sphere showed that the deviations can be further reduced, as nonlinear hydrostatics and viscous drag lead to both excitation and damping of the motion, thereby reducing its dependence on wave height.
- Replacing Gaussian distributions with numerical evaluation led to comparable accuracy and proved that the 4 min time windows are not deviating strongly from a Gaussian distribution.
- Including multiple DOFs led to improved accuracy compared to FD and comparable accuracy compared to single-DOF simulations, but generally higher NRMSE values due to the mooring behavior which was not modeled with SL.

Future work should include an extension of PSWF-SL to more nonlinearities and extend the multiple-DOFs investigation to coupled effects. Executing PSWF-SL for much shorter time windows than 4 min is challenging, since the Gaussian distribution and numerical evaluation are sensitive to outliers. An investigation of the sensitivity of the numerical evaluation without the Gaussian assumption to time window size should be included in future studies. Given that the primary objective of this work is to demonstrate the applicability of integrating the SL approach with wave estimation, the scope has been limited to two representative nonlinear effects. Specifically, Morison drag and nonlinear hydrostatics are considered, corresponding to damping and stiffness contributions in the floater dynamics, respectively. These selections enable a sufficiently comprehensive assessment of the SL technique within the context of this study. Nevertheless, it would be valuable to further assess the performance of this approach by extending the analysis to additional nonlinear effects and non-axisymmetric vessels and comparing to the Kalman Filter or RAO tuning techniques.

Author Contributions: Conceptualization, M.W., J.T. and M.A.-M.; methodology, M.W. and J.T.; validation, M.W. and J.T.; formal analysis, M.W. and J.T.; resources, J.T. and M.A.-M.; data writing—original draft preparation, M.W. and J.T.; writing—review and editing, M.W., J.T. and M.A.-M.; visualization, M.W.; supervision, M.A.-M.; project administration, M.A.-M.; funding acquisition, M.A.-M. All authors have read and agreed to the published version of this manuscript.

Funding: This work was supported by the Bundeswehr Technical Center for Ships and Naval Weapons Maritime Technology and Research; the German Federal Ministry for Economic Affairs and Energy under contract 03SX596B, administered by the Project Management agency Jülich.

Data Availability Statement: The source code for the analysis is available on GitLab: https://collaborating.tuhh.de/m-8/rao_estimator (accessed on 26 April 2026).

Conflicts of Interest: The authors declare no conflicts of interest.

Appendix A. Mathematical Derivation of Statistical Linearization

This appendix outlines the derivation of statistical linearization; further details can be found in [24]. Consider a nonlinear function

$$F_{\text{non}} = f(x), \tag{A1}$$

where x is a zero-mean random variable, and $f(\cdot)$ is a nonlinear function of x. The statistically equivalent linear approximation is assumed to be in the form

$$f_{\text{eq}}(x) = Nx + Q, \tag{A2}$$

where N denotes the equivalent linear coefficient (e.g., $R_{\text{eq,vis}}$, $K_{\text{eq,ext}}$, or $R_{\text{eq,ext}}$ in (3)), and Q represents the mean component of $f(x)$.

The linearization error is defined as

$$\epsilon = f(x) - Nx - Q. \tag{A3}$$

For a stochastic process, the mean-square error is given by

$$\mathbf{E}\left(\epsilon^2\right) = \mathbf{E}\left[(f(x) - Nx - Q)^2\right], \tag{A4}$$

where $\mathbf{E}(\cdot)$ denotes the expectation operator. Minimization of the mean-square error with respect to N and Q requires

$$\frac{\mathrm{d}}{\mathrm{d}N}\mathbf{E}\left(\epsilon^2\right) = 0, \qquad \frac{\mathrm{d}}{\mathrm{d}Q}\mathbf{E}\left(\epsilon^2\right) = 0. \tag{A5}$$

Solving these conditions yields

$$N = \frac{\mathbf{E}[xf(x)]}{\mathbf{E}(x^2)} = \frac{\mathbf{E}[xf(x)]}{\sigma_x^2}, \tag{A6}$$

where σ_u is the standard deviation of u. The numerator can be evaluated as

$$\mathbf{E}[xf(x)] = \int_{-\infty}^{\infty} xf(x)\,p(x)\,\mathrm{d}x, \tag{A7}$$

with $p(x)$ denoting the probability density function of x. Assuming x follows a Gaussian distribution, $p(x)$ is given by

$$p(x) = \frac{1}{\sigma_x\sqrt{2\pi}}\exp\left(-\frac{x^2}{2\sigma_x^2}\right). \tag{A8}$$

Applying (A6) to the nonlinear functions defined in (13) and (18) yields the equivalent linearized coefficients used in this study.

It should be noted that the SL procedure is implemented based on the assumption that the floater as a system follows the Gaussian distribution. As demonstrated in [24], when a linear system is excited by random Gaussian inputs, its responses also tend to be Gaussian distributed. Although incorporating nonlinear effects into the SL approach challenges the assumption of strict linearity, the approach proposed in this work is primarily intended to address operational (non-extreme) wave conditions, where nonlinear contributions are not expected to significantly alter the system dynamics. Moreover, the inertia-dominated behavior of floating structures generally limits strong nonlinear responses, maintaining quasi-linear dynamics under mild-to-moderate sea states. In this context, the SL approach can be adopted as an effective technique to incorporate non-extreme nonlinearities in operations of floating systems, as demonstrated in Section 3.4 and in a few previous studies [15,18,21,23]. Therefore, it is reasonable to assume the dynamics of floaters to be well represented by a Gaussian process in the SL method for non-extreme conditions. Nevertheless, comparative studies between the SL-based approach and higher-fidelity models or experimental data are recommended to identify the limits of applicability, particularly when new nonlinear elements are introduced into dynamic modeling via the SL technique.

References

1. Kim, H.; Kang, H.; Kim, M.H. Real-Time Inverse Estimation of Ocean Wave Spectra from Vessel-Motion Sensors Using Adaptive Kalman Filter. *Appl. Sci.* **2019**, *9*, 2797. [CrossRef]
2. Cademartori, G.; Oneto, L.; Valdenazzi, F.; Coraddu, A.; Gambino, A.; Anguita, D. A review on ship motions and quiescent periods prediction models. *Ocean Eng.* **2023**, *280*, 114822. [CrossRef]
3. Komoriyama, Y.; Iijima, K.; Tatsumi, A.; Fujikubo, M. Identification of wave profiles encountered by a ship with no forward speed using Kalman filter technique and validation by tank tests-long-crested irregular wave case-. *Ocean Eng.* **2023**, *271*, 113627. [CrossRef]
4. Takami, T.; Nielsen, U.D.; Xi, C.; Jensen, J.J.; Oka, M. Reconstruction of incident wave profiles based on short-time ship response measurements. *Appl. Ocean Res.* **2022**, *123*, 103183. [CrossRef]
5. Takami, T.; Nielsen, U.D.; Jensen, J.J.; Chen, X. Estimation of encountered wave elevation sequences based on response measurements in multi-directional seas. *Appl. Ocean Res.* **2023**, *135*, 103570. [CrossRef]
6. Takami, T.; Nielsen, U.D.; Mounet, R.E.G.; Jensen, J.J.; Mori, R.; Komoriyama, Y. Blind identification of incident waves and response transfer functions of a marine vessel based on measured responses. *Expert Syst. Appl.* **2026**, *296*, 129236. [CrossRef]
7. Wermbter, M.; Perić, R.; Serr, J.; Abdel-Maksoud, M. An approach to estimate vertical center of gravity, draught and RAO from ship motions based on prolate spheroidal wave functions and time-series filtering. *Ocean Eng.* **2025**, *341*, 122659. [CrossRef]
8. Guo, B.; Ringwood, J.V. A review of wave energy technology from a research and commercial perspective. *IET Renew. Power Gener.* **2021**, *15*, 3065–3090. [CrossRef]
9. Folley, M. (Ed.) *Numerical Modelling of Wave Energy Converters*; Academic Press: Amsterdam, The Netherlands, 2016.
10. Ransley, E.; Greaves, D.; Raby, A.; Simmonds, D.; Hann, M. Survivability of wave energy converters using CFD. *Renew. Energy* **2017**, *109*, 235–247. [CrossRef]
11. Cummins, W. *The Impulse Response Function and Ship Motions*; Technical Report; David Taylor Model Basin: Washington, DC, USA, 1962.
12. Pastor, J.; Liu, Y. Frequency and time domain modeling and power output for a heaving point absorber wave energy converter. *Int. J. Energy Environ. Eng.* **2014**, *5*, 101. [CrossRef]
13. Mounet, R.E.; Nielsen, U.D.; Brodtkorb, A.H.; Øveraas, H.; Dallolio, A.; Johansen, T.A. Data-driven method for hydrodynamic model estimation applied to an unmanned surface vehicle. *Measurement* **2024**, *234*, 114724. [CrossRef]
14. Nielsen, U.D.; Mounet, R.E.; Brodtkorb, A.H. Tuning of transfer functions for analysis of wave–ship interactions. *Mar. Struct.* **2021**, *79*, 103029. [CrossRef]
15. Folley, M.; Whittaker, T. Spectral modelling of wave energy converters. *Coast. Eng.* **2010**, *57*, 892–897. [CrossRef]
16. Folley, M.; Whittaker, T. Validating a spectral-domain model of an OWC using physical model data. *Int. J. Mar. Energy* **2013**, *2*, 1–11. [CrossRef]
17. Silva, L.S.P.d. Nonlinear Stochastic Analysis of Wave Energy Converters via Statistical Linearization. Ph.D. Thesis, Universidade de São Paulo, São Paulo, Brazil, 2019.
18. Silva, L.; Sergiienko, N.; Pesce, C.; Ding, B.; Cazzolato, B.; Morishita, H. Stochastic analysis of nonlinear wave energy converters via statistical linearization. *Appl. Ocean Res.* **2020**, *95*, 102023. [CrossRef]
19. da Silva, L.S.; Cazzolato, B.S.; Sergiienko, N.Y.; Ding, B.; Morishita, H.M.; Pesce, C.P. Statistical linearization of the Morison's equation applied to wave energy converters. *J. Ocean Eng. Mar. Energy* **2020**, *6*, 157–169. [CrossRef]
20. Spanos, P.D.; Strati, F.M.; Malara, G.; Arena, F. An approach for non-linear stochastic analysis of U-shaped OWC wave energy converters. *Probabilistic Eng. Mech.* **2018**, *54*, 44–52. [CrossRef]
21. Tan, J.; Lavidas, G. A modified spectral-domain model for nonlinear hydrostatic restoring force of heaving wave energy converters. *Ocean Eng.* **2024**, *309*, 118581. [CrossRef]
22. Tan, J.; Tao, W.; Laguna, A.J.; Polinder, H.; Xing, Y.; Miedema, S. A spectral-domain wave-to-wire model of wave energy converters. *Appl. Ocean Res.* **2023**, *138*, 103650. [CrossRef]
23. Tan, J.; Zuo, L.; Lavidas, G.; Metrikine, A. Extending the statistical linearization method to multi-variate non-differentiable nonlinearities in floating renewable energy devices. *Renew. Energy* **2025**, *256* , 123964. [CrossRef]
24. Roberts, J.B.; Spanos, P.D. *Random Vibration and Statistical Linearization*; Courier Corporation: North Chelmsford, MA, USA, 2003.

25. Penalba, M.; Kelly, T.; Ringwood, J. Using NEMOH for modelling wave energy converters: A comparative study with WAMIT. In Proceedings of the 12th European Wave and Tidal Energy Conference (EWTEC), Cork, Ireland, 27 August–1 September 2017.
26. Journée, J.; Massie, W. *Offshore Hydromechanics*; Delft University of Technology: Delft, The Netherlands, 2001; Volume 523.
27. Pérez, T.; Fossen, T. Time-vs. frequency-domain identification of parametric radiation force models for marine structures at zero speed. *Model. Identif. Control* **2008**, *29*, 1–19. [CrossRef]
28. Tan, J.; Polinder, H.; Laguna, A.J.; Miedema, S. A numerical study on the performance of the point absorber Wave Energy Converter integrated with an adjustable draft system. *Ocean Eng.* **2022**, *254*, 111347. [CrossRef]
29. Yu, Y.H.; Lawson, M.; Ruehl, K.; Michelén Ströfer, C. Development and Demonstration of the WEC-Sim Wave Energy Converter Simulation Tool. In Proceedings of the 2nd Marine Energy Technology Symposium, METS 2014, Seattle, WA, USA, 15–18 April 2014.
30. Boyd, J.P. Algorithm 840: Computation of grid points, quadrature weights and derivatives for spectral element methods using prolate spheroidal wave functions—Prolate elements. *ACM Trans. Math. Softw.* **2005**, *31*, 149–165. [CrossRef]
31. Veritas, N. *Environmental Conditions and Environmental Loads*; Det Norske Veritas: Oslo, Norway, 2000.
32. Wendt, F.; Nielsen, K.; Yu, Y.H.; Bingham, H.; Eskilsson, C.; Kramer, M.; Babarit, A.; Bunnik, T.; Costello, R.; Crowley, S.; et al. Ocean Energy Systems Wave Energy Modelling Task: Modelling, Verification and Validation of Wave Energy Converters. *J. Mar. Sci. Eng.* **2019**, *7*, 379. [CrossRef]
33. Giorgi, G.; Ringwood, J.V. Nonlinear Froude-Krylov and viscous drag representations for wave energy converters in the computation/fidelity continuum. *Ocean Eng.* **2017**, *141*, 164–175. [CrossRef]
34. Takami, T.; Dam Nielsen, U.; Juncher Jensen, J.; Maki, A.; Matsui, S.; Komoriyama, Y. Onboard identification of stability parameters including nonlinear roll damping via phase-resolved wave estimation using measured ship responses. *Mech. Syst. Signal Process.* **2024**, *210*, 111166. [CrossRef]

Disclaimer/Publisher's Note: The statements, opinions and data contained in all publications are solely those of the individual author(s) and contributor(s) and not of MDPI and/or the editor(s). MDPI and/or the editor(s) disclaim responsibility for any injury to people or property resulting from any ideas, methods, instructions or products referred to in the content.